The dust and cold gas content of local star-forming galaxies

P. Popesso,[1]★ A. Concas,[2] L. Morselli [ORCID],[3,4] G. Rodighiero,[3,4] A. Enia [ORCID][3,4] and S. Quai [ORCID][5]

[1]*Excellence Cluster Universe, Boltzmannstrasse 2, D-85748 Garching bei München, Germany*
[2]*Kavli Institute for Cosmology, University of Cambridge, Madingley Road, Cambridge CB3 0HA, UK*
[3]*Universitá degli studi di Padova, vicolo dell'Osservatorio, Padova 35122, Italy*
[4]*Osservatorio Astronomico di Padova, vicolo dell'Osservatorio, Padova 35122, Italy*
[5]*University of Victoria, 3800 Finnerty Road, Victoria BC V8P 5C2, Canada*

ABSTRACT

We use dust masses (M_{dust}) derived from far-infrared data and molecular gas masses (M_{mol}) based on CO luminosity to calibrate proxies based on a combination of the galaxy Balmer decrement, disc inclination, and gas metallicity. We use such proxies to estimate M_{dust} and M_{mol} in the local SDSS sample of star-forming galaxies (SFGs). We study the distribution of M_{dust} and M_{mol} along and across the main sequence (MS) of SFGs. We find that M_{dust} and M_{mol} increase rapidly along the MS with increasing stellar mass (M_*), and more marginally across the MS with increasing SFR (or distance from the relation). The dependence on M_* is sub-linear for both M_{dust} and M_{mol}. Thus, the fraction of dust (f_{dust}) and molecular gas mass (f_{mol}) decreases monotonically towards large M_*. The star formation efficiency (SFE, inverse of the molecular gas depletion time) depends strongly on the distance from the MS and it is constant along the MS. As nearly all galaxies in the sample are central galaxies, we estimate the dependence of f_{dust} and f_{gas} on the host halo mass and find a tight anticorrelation. As the region where the MS is bending is numerically dominated by massive haloes, we conclude that the bending of the MS is due to a lower availability of molecular gas mass in massive haloes rather than a lower efficiency in forming stars.

Key words: galaxies: evolution – galaxies: ISM – galaxies: star formation.

1 INTRODUCTION

The interplay between cold gas, dust, and star formation in galaxies plays a key role in the studies of galaxy evolution. Star formation occurs within dense, massive, and cold giant molecular clouds. These are the sites where atomic hydrogen is transformed in molecular hydrogen, while the dust grains act as catalyst of the transformation and shield the site from the UV emission of massive young stars. For this reason, atomic, molecular, and dust mass appear to be correlated quantities and are often used to derive one another in the study of the star formation process in galaxies. Nevertheless, measuring molecular gas (M_{mol}) and dust (M_{dust}) masses in galaxies is a challenging task.

The molecular phase (H_2) is not directly observable (see Kennicutt & Evans 2012, for a review). Therefore, the luminosity due to the $J = 1-0$ transition of the carbon monoxide molecule (CO) is more commonly adopted as a proxy of the H_2 gas mass (e.g. Saintonge et al. 2011; Kennicutt & Evans 2012; Bolatto et al. 2015; Saintonge et al. 2017). Nevertheless, large CO surveys of galaxies are extremely time consuming. The two largest efforts so far have been the Five College Radio Astronomical Observatory

Extragalactic CO Survey (FCRAO; Young et al. 1995), which measured the CO(1–0) line in 300 nearby galaxies, and the IRAM-30m reference CO survey for galaxy evolution studies (xCOLD GASS; Saintonge et al. 2011, 2017), which measured fluxes in the CO(1–0) line for a purely stellar mass selected sample of ∼500 galaxies at $0.025 < z < 0.05$ and stellar masses (M_*) larger than 10^9 M$_\odot$. At higher redshift typical galaxies are now being observed out to $z \sim 0.5$ (e.g. EGNoG; Bauermeister et al. 2013), and further out to $z \sim 2$–3 (e.g. Tacconi et al. 2013; Scoville et al. 2016, 2017), but samples are very small in number at fixed redshift window. With the Atacama Large Millimeter/submillimeter Array (ALMA) the estimates of M_{mol} will surely increase at low and high redshift. However, the small instantaneous field of view of ALMA does not make this instrument suitable for wide area galaxy surveys.

In comparison to M_{mol}, M_{dust} is relatively easier to measure as dust grains emit mainly in the far-infrared (FIR) and sub-millimetre (sub-mm) wavelength range. Early studies of dust content and emission have been done both from space (e.g. IRAS and *ISO*, see Neugebauer et al. 1984; Kessler et al. 1996, respectively) and from the ground (e.g. SCUBA and MAMBO, see Holland et al. 1999; Greve et al. 2008, respectively).

Recent missions in the mid-infrared (e.g. *WISE* and MIPS; Wright et al. 2010; Rieke et al. 2004, respectively), FIR (e.g. HAKARI and *Herschel*; Matsuhara et al. 2006; Pilbratt et al. 2010, respectively),

and sub-mm (e.g. *Planck*; Planck Collaboration I 2011) have revolutionized the field (e.g. Lutz 2014). Cortese et al. (2014) show that as long as the observed SED extends to at least 160–200 μm in the rest frame, M_{dust} can be recovered with a $>3\sigma$ significance and without significant systematic errors. However, mid and FIR instruments as MIPS on-board *Spitzer*, and PACS and SPIRE on-board *Herschel* are no longer available. Furthermore, the existing FIR data are either deep but limited to a small number of objects (the Herschel Reference Survey, ∼300 objects; Boselli et al. 2010) or very shallow, sampling mainly the dustiest objects over large areas (H-ATLAS survey over ∼660 deg^2; Valiante et al. 2016; Smith et al. 2017).

These methods are powerful but they have the important drawback that do not really allow a proper statistical treatment of the distribution of the dust and molecular mass content as a function of galaxy properties, for example along and across the main sequence (MS) of star-forming galaxies (SFGs, e.g. Noeske et al. 2007; Rodighiero et al. 2011; Popesso et al. 2019). Saintonge et al. (2011, 2017) attempt such analysis exploiting data from the xCOLD GASS survey. However, the limited number of galaxies at high stellar masses (less than 100) and hosted by massive dark matter haloes, prevents a proper statistical analysis of the fraction of molecular gas versus M_* and dark matter halo mass (M_{halo}). At higher redshift, Scoville et al. (2016, 2017) provide a similar attempt with ∼1000 galaxies but over a much wider redshift window from $z \sim 1$ to $z \sim 4$. Similarly, the PHIBBS sample (Tacconi et al. 2013; Genzel et al. 2015) covers the same redshift range with a lower number of objects.

More recently, Concas & Popesso (2019) propose an alternative method for measuring M_{mol} in galaxies by exploiting dust *absorption* rather than *emission*. They find a tight correlation between the Balmer decrement (BD, Hα/Hβ), corrected for the galactic disc inclination, the CO luminosity (L_{CO}) and the molecular mass (M_{mol}) with a scatter of ∼0.3 dex. The huge advantage of this method is that the BD is available for statistically significant samples of SFGs, e.g. the SDSS spectroscopic sample in the local Universe. At higher redshift, similar samples will be soon available in huge spectroscopic campaigns with MOONS, PFS, and 4MOST. Thus, the use of the BD as a proxy of M_{mol} and M_{dust} opens up the possibility of studying their distribution in galaxies across a variety of system properties and over a large redshift range, where a complete ALMA follow-up will never be possible.

In this paper, we extend the analysis proposed in Concas & Popesso (2019) on the correlation between the BD and M_{mol}. In addition, we present a correlation between the BD and M_{dust}. We explore, in particular, the role of the galaxy metallicity as possible source of scatter in both the correlations and show the applicability of the BD as proxy of M_{mol} and M_{dust} in a sample of local SFGs drawn from the SDSS spectroscopic sample.

The paper is structured as follows. Section 2 illustrates the data set used in the analysis. Section 3 describes the calibration of the proxies based on BD, inclination and metallicity for M_{dust} and M_{mol}, respectively. Sections 4 shows how the correlations can be used to study the distribution of dust and molecular mass in the local SFGs population. Section 5 shows the relation between the fraction of M_{dust} and M_{mol} with respect to M_{halo}. Section 6 summarizes our results. We assume a ΛCDM cosmology with $\Omega_M = 0.3$, $\Omega_\Lambda = 0.7$, and $H_0 = 70$ km s^{-1} Mpc^{-1}, and a Chabrier IMF throughout the paper.

2 DATA SET

The data set used in this analysis is composed of a local SFG reference sample and two calibration samples. The former is used to study the distribution of dust and molecular gas across and along the MS of SFGs. The latter two are sub-samples of the local SFG reference sample with available M_{dust} and M_{mol} estimates, respectively. They are built to cover the same parameter space and redshift window of the reference sample, and to calibrate the proxies of dust and molecular gas mass, based on the BD, disc inclination, and galaxy metallicity of the SFG reference sample.

2.1 The local star-forming galaxy reference sample

The sample of local SFGs is drawn from the GALEX-SDSS-WISE Legacy Catalog (GSWLC; Salim et al. 2016). GSWLC is obtained by cross-matching the SDSS spectroscopic catalogue with the *GALEX* UV and *WISE* data bases, and also provides SDSS and 2MASS photometric information. It contains galaxies within the *GALEX* footprint, regardless of a UV detection, and is made up of 700 000 galaxies with SDSS redshift between $0.01 < z < 0.30$. We use, in particular, the sub-sample with medium-deep *GALEX* observations of ∼ 1500 s exposure (GSWLC-M), which covers 49 per cent of the SDSS area. This decision was taken to exploit relatively deep UV observations and large statistics. GSWLC utilizes *WISE* observations at 22 μm (*WISE* channel *W*4) to determine SFRs independently of the UV/optical SED fitting. In particular, the mid-IR SFRs in GSWLC are estimated from the total IR luminosity (L_{IR}, 8–1000 μm) by interpolating the luminosity-dependent IR template of Chary & Elbaz (2001) that matches the 22 μm flux. For galaxies undetected in *WISE*, the SFR and dust attenuation are estimated via SED fitting from the UV to the near-IR data. The SED fitting is performed using the state-of-the-art UV/optical SED fitting technique code CIGALE (Noll et al. 2009). The average 5σ depth in the *W*4 channel is 5.4 mJy.

The catalogue is matched to the MPA-JHU data base of galaxy properties[1] to retrieve stellar masses, Hα and Hβ fluxes, the BPT classification and gas metallicity (Kauffmann et al. 2003; Brinchmann et al. 2004; Tremonti et al. 2004; Salim et al. 2007). When the Hα based SFR is available in the MPA-JHU catalogue, we use this estimate to replace the SED fitting based SFR of the GSWLC sample. The match between the GSWLC sample and the MPA-JHU catalogue leads to the selection of ∼350 000 galaxies. However, in order to use the BD as a measure of dust attenuation and so as a proxy of the dust mass and the molecular gas mass, the Hα and Hβ emission must trace only star formation. Indeed, any AGN contamination would bias the Hα and Hβ fluxes and so their ratio, as found in Concas & Popesso (2019). For this reason, we further isolate SFGs on the basis of the BPT classification provided in the MPA-JHU catalogUEs. We further limit the sample to galaxies at $z < 0.1$ in order to have a 80 per cent and 50 per cent spectroscopic completeness above stellar masses of 10^{10} and 10^9 M$_\odot$, respectively. We exclude dwarf galaxies below 10^9, for which the dust/molecular gas properties might significantly differ from more massive SFGs (Cormier et al. 2019).

Prior to the estimate of the BD, we multiply the uncertainties of the Hα and Hβ fluxes by a correction factor ($f = 2.473$ and $f = 1.882$ for the Hα and Hβ line, respectively) to take into account continuum subtraction errors (following Brinchmann et al. 2004). As shown in Concas & Popesso (2019), the BD is a good proxy of M_{mol} once corrected for the galaxy disc inclination. To retrieve an accurate value of the galaxy disc inclination we use the measures provided

---

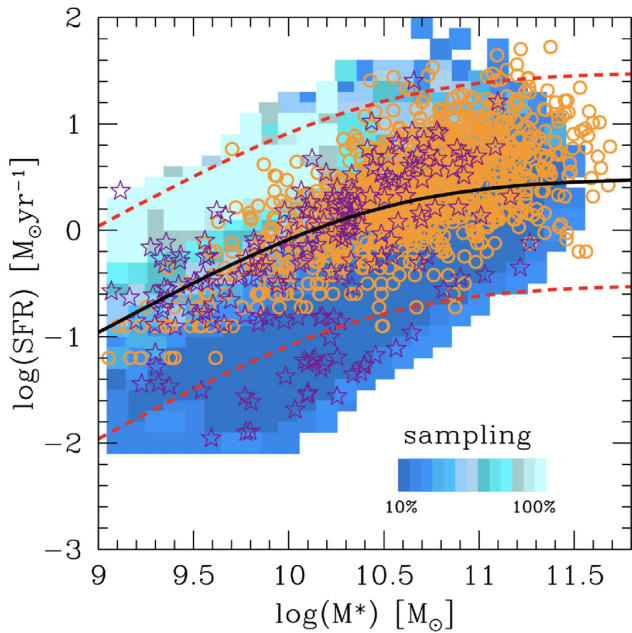[1]https://wwwmpa.mpa-garching.mpg.de/SDSS/DR7/

Figure 1. Distribution and sampling rate of the SF galaxy reference sample with respect to the underlying SF galaxy population in the MS region (shaded region). The colour-code of the shaded region reflect the sampling rate of the SF galaxy reference sample. The orange empty points indicate the location of the dust mass calibration sample, while the purple stars indicate the location of the molecular gas mass calibration sample. The black solid line marks the MS of Popesso et al. (2019), while the dashed red lines are located 3σ above/below the relation.

by the bulge–disc decomposition catalogue of Simard et al. (2011), available for nearly all systems (98 per cent) of the SFG sample.

The final sample comprises ∼150 000 star-forming systems, which we will refer to as the 'SFG reference sample' throughout the paper. As explained in Brinchmann et al. (2004), such SF galaxy sample might induce several biases, because the BPT classification requires a SNR > 3 in several emission lines (H α, H β, N II, and [O III]). The emission line galaxy population selected in this way might not be fully representative of the SFG population in the MS region. To check this aspect, we estimate the sampling rate of the SFG reference sample with respect to the parent GSWLC sample in the same redshift window. The result in shown in Fig. 1. The SFG reference sample populates the whole MS region at all stellar masses within 3σ from the MS relation, taken from Popesso et al. (2019) and estimated exploiting the GSWLC catalogue. However, the sampling rate is not uniform across and along the MS. The SFG reference sample captures a very high percentage (∼50 per cent) of the galaxies above the MS, mainly in the starburst region and in the stellar mass range 10^9–$10^{10.4}$ M$_\odot$. The sampling rate remains quite constant and uniform (17–22 per cent) elsewhere. To correct for this bias we define for each galaxy a weight proportional to the mean sampling rate estimated in a region of 0.2 dex × 0.2 dex in M_* and SFR around each galaxy. These weights are considered when fitting the data in the following sections.

2.2 The calibration samples

2.2.1 Molecular masses

As in Concas & Popesso (2019), the sample of galaxies with available CO luminosity (L_{CO}) is taken from the extended CO

Legacy Database for GASS survey (xCOLD GASS; Saintonge et al. 2017), designed to provide a picture of molecular gas across the local galaxy population. The sample contains 532 galaxies and is obtained by the combination of the original COLD GASS survey, targeting galaxies at $0.025 < z < 0.050$ and $M_* > 10^{10}$ M$_\odot$ (Saintonge et al. 2011), with the COLD GASS-low survey, extended for sources with 10^9 M$_\odot$ < M_* < 10^{10} M$_\odot$ (Saintonge et al. 2017).

A percentage of 63 per cent of the sample (333 objects) is CO detected, while for few of the remaining galaxies upper limits are provided (see Saintonge et al. 2011, 2017). M_{mol} is derived from L_{CO} through the α_{CO} factor conversion, calibrated in Accurso et al. (2017) and dependent on galaxy metallicity. The 532 xCOLD GASS galaxies are cross-matched with the SFG reference sample to retrieve SFRs, M_*, H α, and H β fluxes, disc inclination angles and metallicities. This leads to a sample of 201 star-forming systems: 177 galaxies with detected CO emission and 24 upper limits. The upper limits are combined in a single point of average L_{CO} and M_{mol}.

To complement xCOLD GASS in the starburst region, where the BD might saturate due to the high level of dust content, we include the Herschel SPIRE-selected sample of Bertemes et al. (2018) in the SDSS Stripe 82 area. The shallow *Herschel*-Stripe 82 survey leads to the selection of the dustiest local objects. Bertemes et al. (2018) provide a measure of L_{CO} and M_{mol} for a sub-sample of 78 *WISE* and SPIRE simultaneously detected systems with ALMA follow-up observations of CO. Bertemes et al. (2018) derive M_{mol} from L_{CO} through the α_{CO} factor conversion based on the metallicity calibration of Genzel et al. (2013) and Tacconi et al. (2018). For consistency with the xCOLD GASS data, we re-derive M_{mol} with the α_{CO} factor conversion of Accurso et al. (2017). For this purpose we use the metallicity provided by Bertemes et al. (2018), which is based on the Pettini & Pagel (2004) calibration, as in Accurso et al. (2017). Nevertheless, we point out that the two α_{CO} calibrations lead to consistent results, as already stated in Bertemes et al. (2018). As already shown in Concas & Popesso (2019), the starburst sample follow the BD–L_{CO} and BD–M_{mol} correlations of the xCOLD GASS sample at the highest L_{CO} and M_{mol}.

The sample is cross-matched to the star-forming reference galaxy sample to retrieve SFRs, M_*, H α, and H β fluxes, disc inclination, and metallicities. The match excludes objects at $z > 0.1$ and leads to a subsample of 53 starburst galaxies.

The combination of the xCOLD GASS and Bertemes et al. (2018) starburst samples leads to 220 galaxies with CO detection and 24 upper limits. We refer to this sample throughout the paper as 'the molecular mass calibration sample'. The distribution of these objects in the log(SFR)–log(M_*) plane is shown in Fig. 1 (purple stars). The sample nicely populates the entire MS region. As for the SFG reference sample, to take into account possible biases, we estimate the sampling rate of the calibration sample with respect to the parent GSWLC sample in the same redshift window. We define for each galaxy a weight proportional to the mean sampling rate estimated in a region of 0.2 dex × 0.2 dex in M_* and SFR around each galaxy. These weights are considered when fitting the data in the following sections.

2.2.2 Dust masses

The sample of galaxies with available M_{dust} estimates is obtained combining different Herschel-based surveys. The largest fraction of sources comes from the Herschel Astrophysical Terahertz Large Area Survey (the Herschel ATLAS or H-ATLAS) conducted with *Herschel* PACS and SPIRE. The H-ATLAS is a survey of approx-

imately 660 deg^2 of sky in five photometric bands: 100,160, 250, 350, and 500 μm (Eales et al. 2010). The catalogue used in this work is based on the H-ATLAS DR2 (Maddox et al. 2018). The DR2 covers two H-ATLAS fields at the North and South Galactic Poles for a total area of ∼500 deg^2.

We use the SPIRE emission at 250, 350, and 500 μm to estimate M_{dust}. This is done following the procedure presented in Dunne et al. (2011), by means of a SED fitting with a modified grey-body law $S \propto \nu^\beta B(\nu, T)$ with fixed emissivity index $\beta = 1.5$ in order to retrieve the dust temperature T_{dust}, and then dust masses from

$$M_{dust} = \frac{S_{250} D^2 (1+z) K}{k_{250} B(\nu_{250}, T_{dust})}, \tag{1}$$

where k_{250} is the dust mass absorption coefficient (0.89 m^2 kg^{-1} at 250 μm) and K the K-correction.

As done in previous section, the H-ATLAS catalogue is cross-matched with the SFG reference sample, to retrieve SFRs, M_*, Hα, and Hβ fluxes, BPT classifications, disc inclination and metallicities. This leads to a sample of ∼1200 far-infrared selected star-forming systems.

To complement the H-ATLAS subsample at the low M_{dust} end (as H-ATLAS maps are relatively shallow), we include in our sample the data from the deeper Herschel Reference Survey (HRS; Boselli et al. 2010). The HRS sample is volume limited, containing sources with flux limits in the K band to minimize the selection effects associated with dust and with young high-mass stars and to introduce a selection in stellar mass. Galaxies in HRS span the whole range of morphological types (ellipticals to late-type spirals) and environments (from the field to the centre of the Virgo Cluster). The estimates of M_{dust} are taken from Cortese et al. (2014) and are based on SED fitting of the SPIRE and PACS data. The cross-match between the HRS and our SFG reference samples results in 157 galaxies. The SFG selection limits also the bias towards dense environment due to the inclusion of the Virgo Cluster galaxy population, which is dominated by early-type systems.

Finally, we include the Bertemes et al. (2018) 53 sources in the SDSS Stripe 82 area that have available M_{dust} estimates, matched to the SFG reference sample.

In total we collect a sample of ∼1400 galaxies with M_{dust} measurements based on *Herschel* SPIRE data. We refer to this sample as the 'dust mass calibration sample'. The distribution of the selected objects in the log(SFR)–log(M_*) plane is shown in Fig. 1 (orange empty circles). The sample covers the entire MS region above stellar masses of ∼ 10^{10} M$_\odot$. Below this threshold, most sources lie near the peak of the distribution, while the starburst region is under-represented. As for the molecular mass calibration sample, we estimate a weight for each galaxy on the basis of the sampling rate with respect to the parent GSWLC sample.

3 THE PROXY FOR M_{DUST} AND M_{MOL}

As shown in Concas & Popesso (2019), once corrected for the effect of the disc inclination, the BD is a good proxy of the molecular gas mass. This is because for very inclined galaxies the auto-absorption of the Hα and Hβ emission from the galactic disc tends to saturate the BD and enlarge the scatter of the correlation. In addition to the disc inclination, here we also consider the galaxy metallicity. Concas & Popesso (2019) find a poorly significant correlation between the residuals around the L_{CO}−BD relation and the gas metallicity (Z). However, Z is recognized has a key parameter of the correlation between dust and cold gas in galaxies from the observational (Draine et al. 2007; Muñoz-Mateos et al. 2009) and

Table 1. The table lists the best-fitting values of the fitting form of equation (2) for the dust and the molecular mass.

	α	β	γ	δ
M_{dust}	-6.11 ± 0.02	1.58 ± 0.02	-0.003 ± 0.002	1.46 ± 0.03
M_{mol}	8.72 ± 0.03	4.29 ± 0.02	0.008 ± 0.006	0.65 ± 0.01

the theoretical point of view (Brinchmann et al. 2013). Thus, we include it when calibrating the proxy for M_{dust} and M_{mol}. To find the best proxy, we express log(M_{dust}) and log(M_{mol}) as a function of BD, inclination and metallicity with the following functional form:

$$f(BD, i, Z) = \alpha + \beta * \log(BD - BD_0) + \gamma * (i - i_0) + \delta * Z, \tag{2}$$

where i is the disc inclination angle, BD_0 and i_0 are the mean values of the BD and inclination in the sample, respectively ($BD_0 = 0.63$ and $i_0 = 59$ deg), and $Z = \log(12 + O/H)$ is the gas metallicity. We fit the $\log(M_{dust}) - f_{M_{dust}}(BD, i, Z)$ and $\log(M_{mol}) - f_{M_{mol}}(BD, i, Z)$ relations to retrieve the best-fitting parameters. The fit is performed by weighting each galaxy as explained in Section 2.2 in order to correct for any selection bias. Table 1 lists the best-fitting values and the uncertainties of the four free parameters of equation (2), for M_{dust} and M_{mol}, respectively. In Fig. 2, we show the agreement between the proxies estimated as $f_{M_{dust}}(BD, i, Z)$, $f_{M_{mol}}(BD, i, Z)$ and the observed log(M_{dust}) and log(M_{mol}), respectively. The points scatters around the 1:1 relations with a scatter of 0.24 and 0.22 dex for the $\log(M_{dust}) - f_{M_{dust}}(BD, i, Z)$ and $\log(M_{mol}) - f_{M_{mol}}(BD, i, Z)$ relations, respectively.

The scatter of the $\log(M_{mol}) - f_{M_{mol}}(BD, i, Z)$ relation is slightly smaller than what found in Concas & Popesso (2019), likely because of the introduction of the gas metallicity as additional parameter in the proxy. The distribution of the residuals for both correlations is shown in the bottom panels of Fig. 2. In the right-hand panel of Fig. 2, the mean value of the CO upper limits provided by Saintonge et al. (2017) for the xCOLD GASS sample is indicated by the gold square. This point lies on the best fit as already found in Concas & Popesso (2019).

As a caveat, we point out that the proxies calibrated here for M_{dust} and M_{mol} are applicable only to the SDSS or similar fibre spectroscopy data set with the same fibre aperture, and redshift window. We do not observe significant dependence of the best-fitting residuals on the SDSS fibre aperture of 3 arcsec diameter. However, the BD within the fibre is an average measure of the relative dust reddening of two fluxes and it might change if larger or smaller apertures are considered. We do not attempt here any fibre aperture correction, because the data do not allow to do so. Spatially resolved maps of larger samples of galaxies, such as CALIFA and MaNGA, will allow to study more in detail the dependence of dust and molecular gas content on the BD within the same physical region.

4 THE DUST AND COLD GAS CONTENT ALONG AND ACROSS THE MS

In this section, we use the proxies found in the previous analysis to estimate M_{dust} and M_{mol} for all galaxies in the local SFG reference sample. This allows us to study with unprecedented statistics the distribution of M_{dust} and M_{mol} along and across the MS. To compare our results with others in literature at low (Saintonge et al. 2011, 2017) and high redshift (Tacconi et al. 2013; Scoville et al. 2016, 2017) we parametrize M_{dust} and M_{mol} as a function of M_*, the
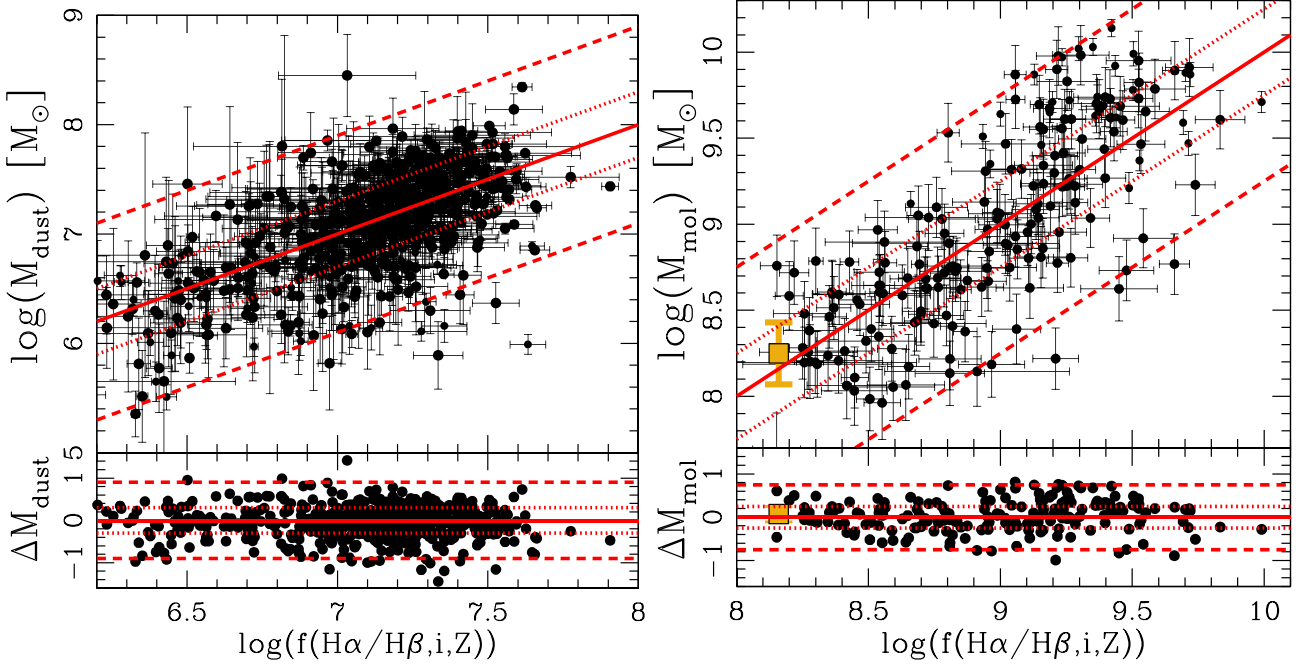
Figure 2. Left-hand panel: The upper panel shows the $\log(M_{dust}) - f_{dust}(BD, i, Z)$ relation. The red solid line shows the 1:1 relation. The dotted line shows the 1σ uncertainty, while the dashed line shows the 3σ level. The bottom panel shows the residual distribution with respect to the 1:1 relation. The red solid, dotted, and dashed lines show the 0 residual level, and the 1 and 3σ scatter around the 1:1 line, respectively. Right-hand panel: Same as in the left-hand panel for the $\log(M_{mol}) - f_{mol}(BD, i, Z)$ relation for the molecular gas calibration sample.

distance from the MS (SFR/SFR_{MS}) and SFR. We use as reference the MS of Popesso et al. ([2019](#)) as it is based on the same SFG reference sample used here. All fits are performed by taking into account the weights of the SFG reference sample in order to correct for undersampling in several regions of the MS. We adopt the following fitting functions:

$$M_{dust} = 10^{\alpha} \times (SFR/SFR_{MS})^{\beta} \times M_*^{\delta}, \tag{3}$$

$$M_{dust} = 10^{\alpha_1} \times SFR^{\beta_1} \times M_*^{\delta_1}. \tag{4}$$

The same fitting forms are assumed for M_{mol}, for the fraction of dust and molecular mass and for the star formation efficiency, defined as $SFE = SFR/M_{mol}$ as in Santini et al. ([2014](#), the inverse of the molecular gas depletion time). In all cases, a combination of M_* and SFR/SFR_{MS} or SFR can reproduce accurately the dust and molecular gas content of SFGs with a scatter varying from 0.19 to 0.22 dex. The best-fitting parameters are provided in Table [2](#) for all the considered variables. The errors are estimated via bootstrapping. Fig. [3](#) shows an example of the best-fitting result for the dust (left-hand panel) and molecular mass (right-hand panel). As a further check, we apply the best-fitting function also to the calibration samples of dust and molecular mass to check if the best fit can reproduce the observed values (green points in the figure). In both cases, the best-fitting functions provide a very good match to the observed dust and molecular masses, with a residual distribution consistent with the reference sample. We observe only a slight asymmetry in the distribution of the residuals for M_{dust}, as shown in the left-hand panel of Fig. [3](#). However, this is not statistically significant. We point out that expressing M_{dust} and M_{mol} as a function of the MS position does not lead to a better fit but it introduces the uncertainties of the MS location. Both dust and molecular masses can be well reproduced as a function of SFR and stellar mass.

The best-fitting results reveal that both M_{dust} and M_{mol} increase as a function of the M_* more rapidly than with the SFR or SFR/SFR_{MS}. M_{dust} exhibits a less significant dependence on the SFR than M_{mol} (see Table [2](#)). In both cases, the dependence on M_* is sub-linear, which implies that the fractions of dust (f_{dust}) and molecular gas masses (f_{mol}) are both decreasing along the MS, by almost two orders of magnitude, as clearly visible in Fig. [4](#). The figure shows the MS region colour-coded as a function of the mean f_{dust} (left-hand panel) and f_{mol} (right-hand panel). It is quite visible that the most significant gradient is along rather than across the relation. Indeed, both f_{dust} and f_{mol} exhibit a poorly significant dependence on SFR or SFR/SFR_{MS}, as indicated in Table [2](#). The lowest fraction of M_{dust} and M_{mol} is reached where the MS bends towards higher masses.

Our results are qualitatively in agreement with previous studies, but we point out a quantitative discrepancy. Saintonge et al. ([2011](#)) find very similar results on the basis of the xCOLD GASS sample. However, they report that the fraction of molecular gas depends mainly on the galaxy specific SFR ($sSFR = SFR/M_*$). Instead, the different dependence on M_* and SFR found here implies that sSFR is not the best proxy. Indeed, when fitting f_{mol} as a function of the sSFR we obtain a decent fit but with a much larger scatter (0.41 dex), with respect to the fitting form of equation (4). We speculate that the discrepancy of the results might be induced by the limited number of galaxies of the xCOLD GASS sample with respect to the statistics offered by our SFG reference sample. An additional source of discrepancy is that Saintonge et al. ([2017](#)) is based on the stacking analysis of the IRAM spectra in several regions of the $\log SFR$–$\log M_*$ plane. Thus, the discrepancy might also arise from averaging M_{mol} and f_{mol} in bins of SFR and M_* rather than considering the full sample.

Scoville et al. ([2016](#)), Scoville et al. ([2017](#)) find, at much higher redshift, that M_{mol} increases in the same way with M_* and SFR/SFR_{MS} as $\propto SFR/SFR_{MS}^{0.32} * M_*^{0.3}$. Despite the quantitative

Table 2. The table lists the best-fitting parameters of the fitting forms given in equations (3) and (4) for M_{dust}, M_{mol}, f_{dust}, f_{mol}, and SFE, respectively.

	$10^{\alpha} \times (SFR/SFR_{MS})^{\beta} \times M_*^{\delta}$				$10^{\alpha_1} \times SFR^{\beta_1} \times M_*^{\delta_1}$			
	α	β	δ	σ	α_1	β_1	δ_1	σ
M_{dust}	1.87 ± 0.01	0.12 ± 0.01	0.50 ± 0.01	0.22	0.78 ± 0.02	0.04 ± 0.01	0.62 ± 0.01	0.20
M_{mol}	2.99 ± 0.01	0.15 ± 0.01	0.58 ± 0.02	0.21	2.61 ± 0.01	0.11 ± 0.01	0.61 ± 0.02	0.23
f_{dust}	2.03 ± 0.01	0.097 ± 0.01	-0.51 ± 0.01	0.23	0.86 ± 0.02	0.01 ± 0.01	-0.39 ± 0.01	0.20
f_{mol}	3.34 ± 0.01	0.10 ± 0.01	-0.45 ± 0.01	0.21	2.88 ± 0.02	0.05 ± 0.01	-0.40 ± 0.01	0.20
SFE	-10.25 ± 0.01	0.88 ± 0.02	0.11 ± 0.01	0.14	-3.48 ± 0.02	0.87 ± 0.02	-0.52 ± 0.01	0.20
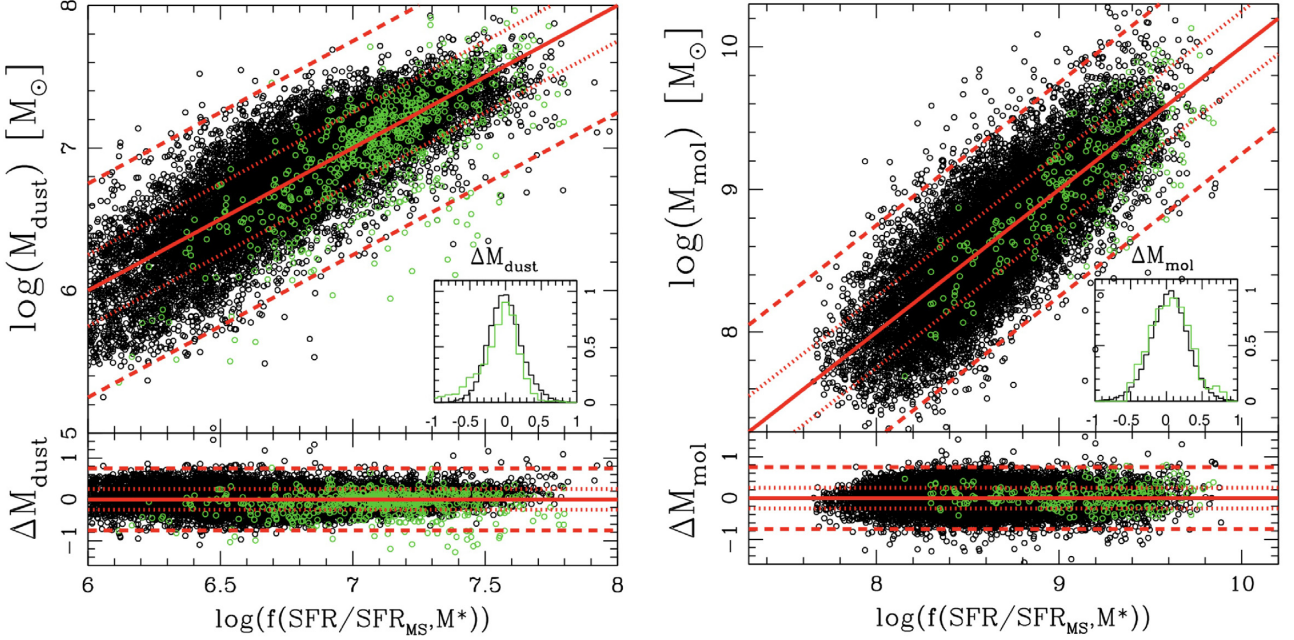
Figure 3. Left-hand panel: The upper panel shows how well M_{dust} can be expressed as a function of SFR/SFR$_{MS}$ and M_* according to equation (3). The black points show the SFG reference sample. The green points shows to the dust mass calibration sample. The red solid, dotted, and dashed lines show the 1:1 relation, and the 1 and 3σ levels, respectively. The small panel shows the histograms of the residual distributions (black for the SFG reference sample, green for the calibration sample). The bottom panel shows the residual distribution with respect to the 1:1 relation. The red solid, dotted, and dashed lines show the 0 residual level, and the 1 and 3σ levels, respectively. The points are colour-coded as in the upper panel. Right panel: same as in the left-hand panel for log(M_{mol}). In these panels, the green points show the molecular mass calibration sample.

discrepancy, the relation of Scoville et al. (2017) suggests, as our findings, that f_{mol} decreases much faster with the M_* than with SFR. So they also find that sSFR cannot be the key parameter in expressing M_{mol} or f_{mol}. The same level of agreement is found also with the results of Santini et al. (2014).

We also estimate the SFE and study how this quantity varies along and across the MS. According to the best fits of equations (3) and (4), SFE is the only parameter, for which the use of the equation (3) leads to a smaller scatter (0.14 dex), with respect to equation (4) (0.2 dex). In addition, once the distance from the MS is considered, the dependence on the stellar mass becomes negligible, as reported in Table 2. Fig. 5 shows the MS region colour-coded as a function of the mean SFE. It is quite visible that the location of the MS is characterized by a constant value of SFE, which increases rapidly as a function of the distance from the MS (SFE $\propto$ SFR/SFR$_{MS}^{0.88}$). The value of SFE on the MS is $\sim 1.05 \pm 0.3 \times 10^{-9}$ yr^{-1}, which is consistent with the average depletion time (1/SFE, e.g. the time needed to consume the available gas mass) estimated for the xCOLD GASS sample in Saintonge et al. (2013). SFE varies by almost four order of magnitudes across the MS over the 3σ region around the relation.

This is consistent with previous results in literature, which find that the depletion time depends mainly on the distance from the

MS, both at low (Saintonge et al. 2013) and high redshift (Tacconi et al. 2013; Genzel et al. 2015; Scoville et al. 2017). Schreiber et al. (2015) find, instead, that SFE decreases at large stellar masses at $z \sim$ 1, and it is the cause for the bending of the relation. The discrepancy might arise from the method used to estimate the gas mass. Schreiber et al. (2015) use the dust-to-gas mass ratio, corrected for the gas metallicity. This is a proxy for the total gas mass ($M_{HI} + M_{H2}$), including atomic and molecular phases. Here, instead, we calibrate our proxy only to provide the mass of the molecular gas phase, similarly to the literature results cited above.

We conclude that the lower fraction of dust and molecular gas mass at the high-mass end, rather than a lower efficiency in forming stars, is more likely to explain the bending of the MS. The reduced availability of fuel for the star formation process, would lead, indeed, to a lower SFR in galaxies, consistently with the results obtained by Saintonge et al. (2017).

5 A TIGHT RELATION WITH THE HOST HALO MASS

Popesso et al. (2019) find that the MS region is dominated by central galaxies over a wide range of stellar masses. Below 10^{10} M$_\odot$,
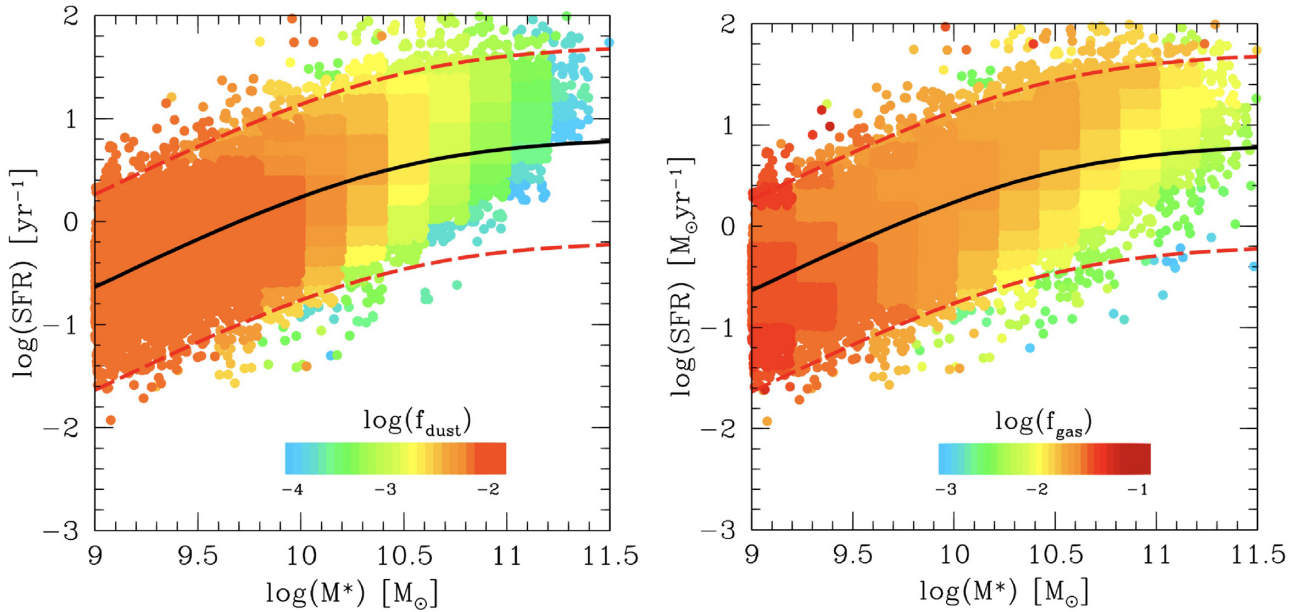
Figure 4. Left-hand panel: Distribution of the SFG reference sample colour-coded as a function of the dust mass fraction (f_{dust}). The colour-code is indicated in the figure. Right-hand panel: Distribution of the SFG reference sample colour-coded as a function of the dust mass fraction (f_{mol}). The colour code is indicated in the figure.
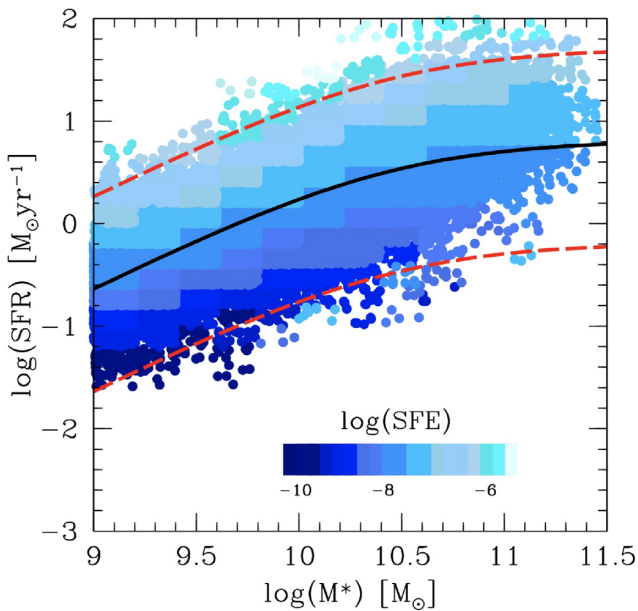

Figure 5. Distribution of the SFG reference sample colour-coded as a function of SFE. Each bin is colour-coded as a function of the average SFE in the bin.

the relation is dominated by central galaxies of low-mass haloes with masses below 10^{12}–$10^{12.5}$ M$_\odot$. Above the same stellar mass threshold, the MS region is populated mostly by star-forming central galaxies of low- and high-mass groups from 10^{13} to 10^{14} M$_\odot$. The few star-forming giant BCGs occupy the tail of the relation at high stellar masses. This distribution suggests a relation between the MS and the host halo mass, likely due to the tight correlation between the central galaxy stellar mass, $M_{*,c}$, and its host halo mass, M_{halo} (e.g. Moster et al. 2010; Behroozi, Wechsler & Conroy 2013; Yang et al. 2017). Indeed, Popesso et al. (2019) show also that SFGs

at the centre of haloes with mass larger than 10^{12} $M_\odot$ dominate numerically the MS in the region where the relation is bending. In this section, we investigate whether there is a more general relation between the baryonic mass content of galaxies and their M_{halo}, able to explain the reduced availability of dust and molecular mass at the high-mass end of the MS.

We check this aspect by matching the SFG reference sample with the M_{halo} catalogue of Yang et al. (2005). This catalogue is based on SDSS DR7 and it provides a classification of galaxies in central/satellites and a measure of M_{halo}. A percentage of 93 per cent of the reference sample has a match in the Yang et al. (2005) catalogue. Of this 89 per cent are classified as central galaxies. The halo mass is estimated through the correlation between the total group and cluster luminosity in the SDSS r band (L_r) and the halo mass. L_r is estimated as the sum of the luminosities of the group members above a fixed absolute magnitude. The calibration of L_r as a proxy for M_{halo} in Yang et al. (2005) holds down to halo masses of $10^{11.5}$ M$_\odot$. To extend the halo mass info down to lower masses, namely for isolated galaxies with stellar mass below $10^{9.5}$ M$_\odot$, we estimate the mass of the host halo through the $M_{*,c}$–M_{halo} relation of Behroozi et al. (2013). To further check our results, we also use, as alternative halo mass estimate, the M_{halo} derived by Tempel et al. (2014), based on the group velocity dispersion and under the assumption of a NFW profile.

Fig. 6 shows how f_{dust} (blue points) and f_{mol} (black points) vary as a function of the M_{halo}. We find a very tight and significant anticorrelation for both quantities, which decrease by more than an order of magnitude from galaxies inhabiting 10^{11} M$_\odot$ haloes to those in massive groups and clusters, with masses larger than 10^{14} M$_\odot$. The best-fitting power law is $f_{dust} \propto M_{halo}^{-0.36 \pm 0.02}$ and $f_{dust} \propto M_{halo}^{-0.31 \pm 0.03}$ The scatter is 0.19 and 0.21 dex for the f_{dust}–M_{halo} and the f_{mol}–M_{halo} relations, respectively. This would suggest that central galaxies of group and clusters are very inefficient in accreting or retaining their dust and molecular mass content with respect to galaxies at the centre of lower mass haloes. Interestingly, while f_{dust} and f_{mol} decrease rapidly with M_{halo}, the
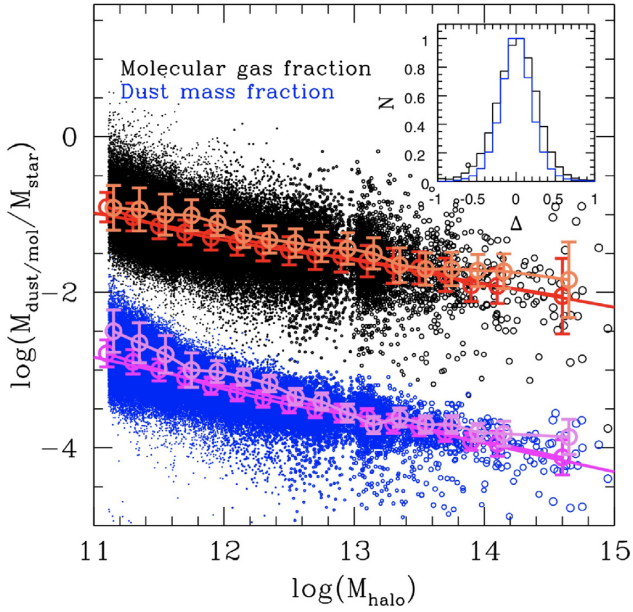
Figure 6. Dust (blue points) and molecular gas fractions (black points) as a function of $M_{\rm halo}$ for all the central galaxies of the SFG reference sample (89 per cent of the sample).The magenta and red points show the median $f_{\rm dust}-M_{\rm halo}$ and $f_{\rm mol}-M_{\rm halo}$ relations, respectively, based on the halo mass estimates of Yang et al. (2007). The orange and violet points show the same relations, respectively, based on the halo masses of Tempel et al. (2014).
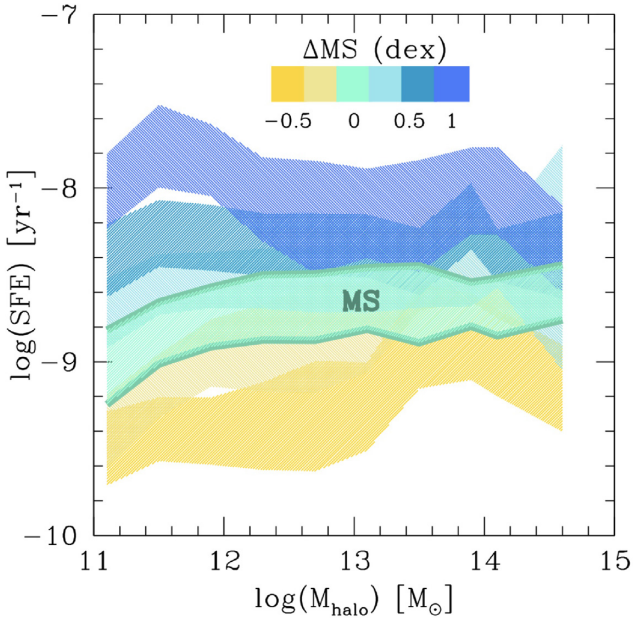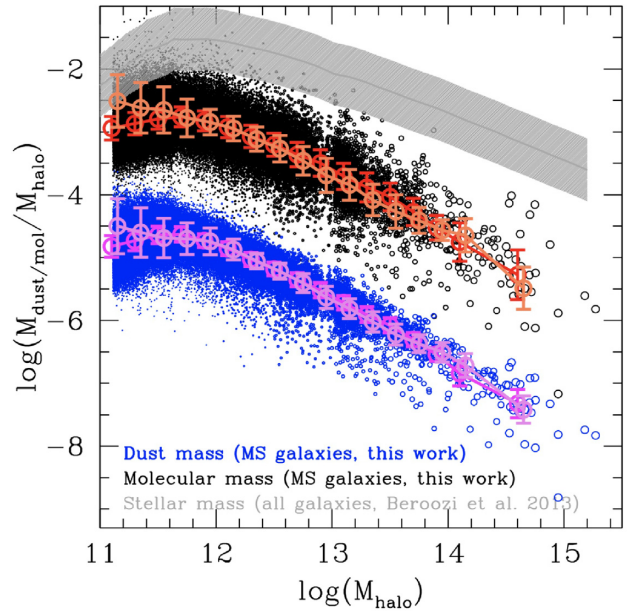

Figure 8. Relation between the fraction of dust mass (blue points) and molecular mass (black points) over the host halo mass as a function of the host halo mass ($M_{\rm halo}$) for the central galaxies of the SFG reference sample. The magenta and red connected empty points show the median $M_{\rm dust}/M_{\rm halo}-M_{\rm halo}$ and $M_{\rm mol}/M_{\rm halo}-M_{\rm halo}$ relations, based on the halo masses estimated by Yang et al. (2007). The orange and violet points show the same relations, respectively, based on the halo masses of Tempel et al. (2014). The shaded region shows the $M_*/M_{\rm halo}-M_{\rm halo}$ relation of Behroozi et al. (2013).
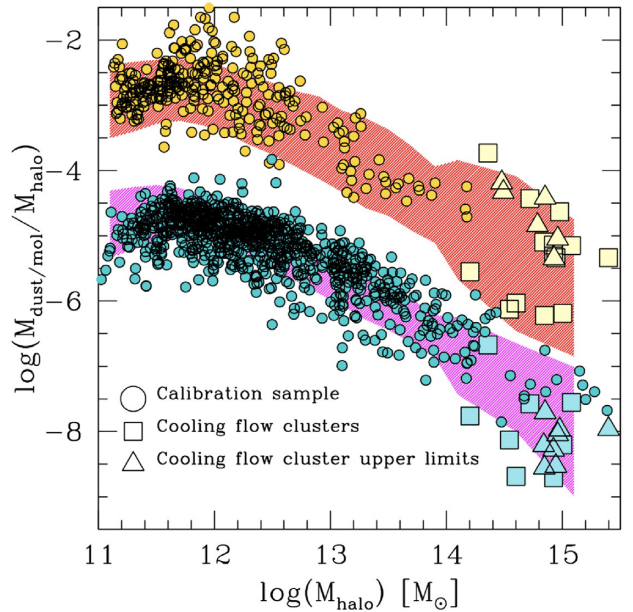

Figure 7. Relation the SFE and the host halo mass. The different shaded regions indicate different bins of distance from the MS (SFR/SFR$_{\rm MS}$), colour-coded as indicated in the figure.

SFE does not show any dependence on $M_{\rm halo}$, and it remains constant, at fixed distance from the MS, over the whole dynamic mass range considered here (see Fig. 7). These results are not surprising, if we consider that $M_{\rm halo}$ and M_* are strongly correlated for central galaxies and that both $M_{\rm dust}$ and $M_{\rm mol}$ exhibit the strongest dependence on the stellar mass rather than the SFR (see Table 2).

Figure 9. $M_{\rm dust}/M_{\rm halo}-M_{\rm halo}$ (magenta region) and $M_{\rm mol}/M_{\rm halo}-M_{\rm halo}$ (red region) relations as in Fig. 8, with overplotted the dust mass (cyan points) and molecular gas (yellow points) calibration samples, respectively. The dashed regions indicates the 3σ regions of the relations. The squares indicate the dust (blue symbols) and molecular gas (yellow symbols) mass estimates of the cooling flow cluster sample of Edge (2001). The triangles indicate the upper limits in the same sample, colour-coded as the squares.

Table 3. The table lists the sample of cooling flow clusters, collected in Edge (2001) with detection of dust and CO emission in the central galaxy. The dust and molecular mass estimates and upper limits are taken from the calibration of Edge (2001). All references for the individual detections can be found in that work. The cluster masses are estimated through different methods: (^{a}): cluster mass derived through mass–temperature relation of Finoguenov, Reiprich & Böhringer (2001). The temperature is derived from Ebeling et al. (1998, 2000). The relation provide M_{500}, which is converted into M_{200} assuming an NFW profile with a concentration parameter computed from the relation of Macciò et al. (2007); (^{b}): cluster mass derived from Hatch, Crawford & Fabian (2007); (^{c}): cluster mass derived through X-ray luminosity (L_X)–mass relation of Rykoff et al. (2008). L_X is derived from Stott et al. (2008); (^{d}): cluster mass estimate of Lu et al. (2010); (^{e}): cluster mass measure of Medezinski et al. (2010); (^{f}): cluster mass derived through L_X–mass relation of Rykoff et al. (2008), with L_X taken from Green et al. (2017); (^{g}): cluster mass derived from Ettori, Fabian & White (1998).

Cluster	Redshift	Mass ($10^{14}\,M_\odot$)	$M_{\rm dust}$ ($M_\odot$)	$M_{\rm mol}$ ($M_\odot$)
A262	0.0171	1.60^a	4.4×10^6	$9 \pm 1.3 \times 10^8$
RXJ0352+19	0.109	8.38^a	$<6.9 \times 10^6$	$1.2 \pm 10.3 \times 10^{10}$
A478	0.0882	10.10^a	1×10^7	$1.3 \pm 1 \times 10^9$
RXJ0439+05	0.208	18.70^a	$<3.1 \times 10^7$	$<3.3 \times 10^{10}$
A646	0.1268	9.10^a	$<1.3 \times 10^7$	$<1.3 \times 10^{10}$
RXJ0821+07	0.110	5.25^b	2.2×10^7	$3.9 \pm 0.4 \times 10^{10}$
Zw2089	0.235	16.6^a	$<4.2 \times 10^7$	$<4.6 \times 10^{10}$
Hydra-A	0.052	4^a	1.3×10^6	$7.4 \pm 1 \times 10^8$
Zw3146	0.2906	30^a	2.2×10^8	$1.6 \pm 0.3 \times 10^{11}$
A1068	0.1386	2.29^a	7.7×10^7	8.5×10^{10}
Zw3916	0.204	10.5^c	$<3.5 \times 10^8$	$<1.6 \times 10^{10}$
A1664	0.1276	9.46^c	$<1.6 \times 10^7$	$4.4 \pm 0.7 \times 10^{10}$
RXJ1347−11	0.4503	16^d	1.8×10^8	$<6.8 \times 10^{10}$
A1795	0.0620	7^a	$<3.1 \times 10^6$	$8.4 \pm 1 \times 10^8$
A1835	0.2523	31.8^a	1×10^8	$1.8 \pm 0.2 \times 10^{11}$
Zw7160	0.2578	17.2^a	1.5×10^8	$6.1 \pm 2.4 \times 10^{10}$
RXJ1532+30	0.3615	28.9^a	$<1.2 \times 10^8$	$2.5 \pm 0.4 \times 10^{11}$
A2146	0.2343	8.5^e	5.6×10^7	$<3.5 \times 10^{10}$
A2204	0.1514	25^a	$<4.3 \times 10^7$	$2.3 \pm 0.6 \times 10^{10}$
Zw8193	0.1825	7.09^f	$<2.2 \times 10^7$	$<4.3 \times 10^{10}$
Zw8197	0.1140	6.9^f	$<6.7 \times 10^6$	$1.1 \pm 0.3 \times 10^{10}$
Zw8276	0.0757	8.4^a	2.6×10^6	$8.2 \pm 1.2 \times 10^9$
A2390	0.2328	28^a	9×10^7	$<4.9 \times 10^{10}$
A2597	0.0852	8.8^f	$<4.1 \times 10^6$	$8.1 \pm 3.3 \times 10^9$
NGC 1275	0.0184	12^g	5.3×10^7	$1.7 \pm 0.2 \times 10^{10}$
IRAS09104+4109	0.4420	8.2^a	1.6×10^8	$<5.1 \times 10^{10}$
A1367	0.0218	3.5^a	4.1×10^6	$5.2 \pm 1 \times 10^8$
A2029	0.079	8.47^a	–	$<6 \times 10^9$
A2199	0.03	6.1^a	–	$<1.4 \times 10^{10}$
2A0335	0.0349	3^a	–	$<3.1 \times 10^{10}$
A2052	0.03	3.1^a	–	$<2.3 \times 10^{10}$

Similarly to what done in Behroozi et al. (2013, 2019) for the efficiency of stellar mass growth, we estimate the efficiency in accreting/retaining the dust and molecular gas content as the fraction of dust and molecular gas over the host halo mass, for all central galaxies. Namely, we define the $M_{\rm dust}/M_{\rm halo}-M_{\rm halo}$ and $M_{\rm mol}/M_{\rm halo}-M_{\rm halo}$ relations in a similar way to the $M_{*,c}/M_{\rm halo}-M_{\rm halo}$ relation. These are shown in Fig. 8. For comparison we plot also the $M_{*,c}/M_{\rm halo}-M_{\rm Halo}$ relation of Behroozi et al. (2013, grey shaded region). The shapes of the two relations resemble the $M_{*,c}/M_{\rm halo}-M_{\rm Halo}$ relation. Although our data do not go beyond halo masses of $10^{11}\,M_\odot$, we can clearly see a peak at $10^{11.7}-10^{11.9}\,M_\odot$ and a monotonically decreasing function towards larger masses, when using the Yang et al. (2005) catalogue (red end magenta points in Fig. 8). In this case, the best power-law fit at masses larger than $10^{12}\,M_\odot$ is of the form $\propto M_{\rm halo}^{-0.5}$ for both $M_{\rm dust}/M_{\rm halo}$ and $M_{\rm mol}/M_{\rm halo}$. Nevertheless, we point out that the position of the peak is very uncertain. Indeed, the halo mass estimates of Tempel et al. (2014) lead to a consistent relation within 1σ above $M_{\rm halo}$ of $10^{12}\,M_\odot$, but with a less evident peak. Below the peak towards

lower $M_{\rm halo}$, $M_{\rm dust}/M_{\rm halo}$ and $M_{\rm mol}/M_{\rm halo}$ tend to decrease. However, our stellar and halo mass limit and the uncertainty in the peak position prevents from robustly confirming the exact shape of the relation in this halo mass regime.

We underline that this relation is valid only for SFGs, where the proxies for $M_{\rm dust}$ and $M_{\rm mol}$ can be estimated. We speculate that the scatter of the relation should become larger in the regime of groups and clusters, which host predominantly inactive galaxies.

To further check the reliability of such relations, we plot them in Fig. 9 as shaded regions, together with the dust and molecular mass calibration samples (cyan and yellow circles, respectively). In both cases, the calibration samples lie in the region of the relations, although they undersample the group and cluster mass regime. To check the relation in the cluster regime ($M_{\rm halo} > 10^{14}\,M_\odot$), we plot the $M_{\rm dust}/M_{\rm halo}$ and $M_{\rm mol}/M_{\rm halo}$ of the cooling flow cluster BCG sample of Edge (2001). The sample is a collection of massive cooling flow systems with a central SFG, with dust and CO-based molecular mass estimate. The properties of the sample, including cluster name, redshift, $M_{\rm halo}$, $M_{\rm dust}$, and $M_{\rm mol}$ (or upper limits) are

reported in Table 3 with all the relative references (in the caption). All systems lie within the 3σ regions of the $M_{dust}/M_{halo}-M_{halo}$ and $M_{mol}/M_{halo}-M_{halo}$ relations. The data are consistent with the shape, scatter and the slope of the relations also in the cluster regime.

We conclude that both dust and molecular gas contents of SFGs in the MS region are strictly related to the mass of the host halo. Thus, the relation between central galaxy and host halo does not affect only the stellar mass content but more in general the galaxy baryonic mass content. The progressive decrease of M_{dust}/M_{halo} and M_{mol}/M_{halo} towards the group and cluster dynamical range, indicate that such extreme environments are inhospitable sites to the SF process due to the lack of availability of molecular gas.

6 SUMMARY AND CONCLUSIONS

We summarize here the findings of our analysis. We first investigate how the a combination of BD, disc inclination, and gas metallicity correlates with the dust and molecular masses in a sample of SFGs. We then use these proxies to estimate the dust and molecular masses for a large sample of local SDSS SFGs at $z < 0.1$. With these estimates available, we study the distribution of the dust and molecular mass along and across the MS relation of SGFs.

The dust and molecular gas content can be expressed as a function of the SFR, or the distance from the MS, and the stellar mass. Both M_{dust} and M_{mol} tend to increase faster along the MS with the stellar mass than across the MS with the SFR or the distance from the MS. The dependence on the stellar mass is, in both cases, sub-linear. This implies that the fractions of dust and molecular mass content are decreasing along the MS, while they increase across the MS with the SFR. The different dependence on SFR and stellar mass implies also that the specific sSFR alone cannot be a good proxy for M_{dust} and M_{mol} or their fractions. Similarly we find that the SFE (inverse of the depletion time) is nearly constant along the MS and it depends marginally on the stellar mass and very significantly on the distance from the MS. SFE varies by more than four orders of magnitudes across the entire 3σ MS region.

We also define the fraction of dust and molecular mass with respect to the halo mass as a measure of the halo efficiency in accreting or retaining their dust and molecular gas content. Such efficiency recalls the shape of the $M_{*,c}/M_{halo}-M_{halo}$. The maximum is reached for central galaxies inhabiting haloes of $10^{11.7}-10^{11.9}$ $M_\odot$ and it decreases by more than two orders of magnitude towards group- and cluster-sized haloes. Conversely, the SFE is constant as a function of the halo mass and depends only on the distance from the MS. As the region where the MS is bending is numerically dominated by such massive haloes, we conclude that the bending is due to a lower availability of baryonic mass in massive haloes rather than a lower efficiency in forming stars.

DATA AVAILABILITY

The data underlying this article are available at the SDSS data base (https://www.sdss.org/dr16/), the MPA-JHU data base of galaxy properties (https://www.mpa.mpa-garching.mpg.de/SDSS/DR7/), the CO Legacy Database for GASS survey (http://www.star.ucl.ac.uk/xCOLDGASS/data.html), the Herschel SPIRE-selected sample of Bertemes et al. (2018), the H-ATLAS DR2 (https://www.h-atlas.org/public-data/download), and the Herschel Reference Survey (https://hedam.lam.fr/HRS/).

REFERENCES

Accurso G. et al., 2017, MNRAS, 470, 4750
Bauermeister A. et al., 2013, ApJ, 768, 132
Behroozi P. S., Wechsler R. H., Conroy C., 2013, ApJ, 762, L31
Behroozi P., Wechsler R. H., Hearin A. P., Conroy C., 2019, MNRAS, 488, 3143
Bertemes C. et al., 2018, MNRAS, 478, 1442
Bolatto A. D. et al., 2015, ApJ, 809, 175
Boselli A. et al., 2010, PASP, 122, 261
Brinchmann J., Charlot S., White S. D. M., Tremonti C., Kauffmann G., Heckman T., Brinkmann J., 2004, MNRAS, 351, 1151
Brinchmann J., Charlot S., Kauffmann G., Heckman T., White S. D. M., Tremonti C., 2013, MNRAS, 432, 2112
Chary R., Elbaz D., 2001, ApJ, 556, 562
Concas A., Popesso P., 2019, MNRAS, 486, L91
Cormier D. et al., 2019, A&A, 626, A23
Cortese L. et al., 2014, MNRAS, 440, 942
Draine B. T. et al., 2007, ApJ, 663, 866
Dunne L., 2011, MNRAS, 417, 1510
Eales S. et al., 2010, PASP, 122, 499
Ebeling H., Edge A. C., Bohringer H., Allen S. W., Crawford C. S., Fabian A. C., Voges W., Huchra J. P., 1998, MNRAS, 301, 881
Ebeling H., Edge A. C., Allen S. W., Crawford C. S., Fabian A. C., Huchra J. P., 2000, MNRAS, 318, 333
Edge A. C., 2001, MNRAS, 328, 762
Ettori S., Fabian A. C., White D. A., 1998, MNRAS, 300, 837
Finoguenov A., Reiprich T. H., Böhringer H., 2001, A&A, 368, 749
Genzel R. et al., 2013, ApJ, 773, 68
Genzel R. et al., 2015, ApJ, 800, 20
Green T. S. et al., 2017, MNRAS, 465, 4872
Greve T. R., Pope A., Scott D., Ivison R. J., Borys C., Conselice C. J., Bertoldi F., 2008, MNRAS, 389, 1489
Hatch N. A., Crawford C. S., Fabian A. C., 2007, MNRAS, 380, 33
Holland W. S. et al., 1999, MNRAS, 303, 659
Kauffmann G. et al., 2003, MNRAS, 341, 54
Kennicutt R. C., Evans N. J., 2012, ARA&A, 50, 531
Kessler M. F. et al., 1996, A&A, 315, L27
Lu T. et al., 2010, MNRAS, 403, 1787
Lutz D., 2014, ARA&A, 52, 373
Macciò A. V., Dutton A. A., van den Bosch F. C., Moore B., Potter D., Stadel J., 2007, MNRAS, 378, 55
Maddox S. J. et al., 2018, ApJS, 236, 30
Matsuhara H. et al., 2006, PASJ, 58, 673
Medezinski E., Broadhurst T., Umetsu K., Oguri M., Rephaeli Y., Benítez N., 2010, MNRAS, 405, 257
Moster B. P., Somerville R. S., Maulbetsch C., van den Bosch F. C., Macciò A. V., Naab T., Oser L., 2010, ApJ, 710, 903
Muñoz-Mateos J. C. et al., 2009, ApJ, 701, 1965
Neugebauer G. et al., 1984, ApJ, 278, L1
Noeske K. G. et al., 2007, ApJ, 660, L47
Noll S., et al., 2009, A&A, 507, 1743
Pettini M., Pagel B. E. J., 2004, MNRAS, 348, L59
Pilbratt G. L. et al., 2010, A&A, 518, L1
Planck Collaboration I, 2011, A&A, 536, A1
Popesso P. et al., 2019, MNRAS, 483, 3213
Rieke G. H. et al., 2004, ApJS, 154, 25
Rodighiero G. et al., 2011, ApJ, 739, L40
Rykoff E. S. et al., 2008, MNRAS, 387, L28
Saintonge A. et al., 2011, MNRAS, 415, 32
Saintonge A. et al., 2013, ApJ, 778, 2
Saintonge A. et al., 2017, ApJS, 233, 22
Salim S. et al., 2007, ApJS, 173, 267

Salim S. et al., 2016, ApJS, 227, 2

Santini P. et al., 2014, A&A, 562, A30

Schreiber C. et al., 2015, A&A, 575, A74

Scoville N. et al., 2016, ApJ, 820, 83

Scoville N. et al., 2017, ApJ, 837, 150

Simard L., Mendel J. T., Patton D. R., Ellison S. L., McConnachie A. W., 2011, ApJS, 196, 11

Smith M. W. L. et al., 2017, ApJS, 233, 26

Stott J. P., Edge A. C., Smith G. P., Swinbank A. M., Ebeling H., 2008, MNRAS, 384, 1502

Tacconi L. J. et al., 2013, ApJ, 768, 74

Tacconi L. J. et al., 2018, ApJ, 853, 179

Tempel E. et al., 2014, A&A, 566, A1

Tremonti C. A. et al., 2004, ApJ, 613, 898

Valiante E. et al., 2016, MNRAS, 462, 3146

Wright E. L. et al., 2010, AJ, 140, 1868

Yang X., Mo H. J., van den Bosch F. C., Jing Y. P., 2005, MNRAS, 356, 1293

Yang X., et al., 2007, ApJ, 671, 153

Yang X. et al., 2017, ApJ, 848, 60

Young J. S. et al., 1995, ApJS, 98, 219

This paper has been typeset from a TEX/LATEX file prepared by the author.